Free-Flight Measurements of Static Aerodynamic Coefficients on a Complex Body

Andrew Hyslop * , Luke J. Doherty † and Matthew McGilvray ‡
Oxford Thermofluids Institute, University of Oxford, Oxford, United Kingdom, OX2 0ES

The measurement of high quality force coefficients in the hypersonic regime within short duration wind tunnels is challenging, particularly for complex geometries. In this study, the static free-flight force measurement technique has been applied to a finned 7 degree half-angle cone within the University of Oxford High Density Tunnel at a flight-representative Mach 7 condition. A quasi-static free-flight test is achieved by matching the locations of the centre of gravity and centre of pressure reducing the static margin of the body and hence the amount of pitching motion. Static free-flight becomes more difficult for complex bodies where the centre of pressure is a function of angle of attack. Longitudinal static force and moment coefficients were measured at the Mach 7 condition with the experimental data agreeing well with numerical predictions. Forces were obtained using both image tracking at 76,000 fps as well as the direct measurement of accelerations using an on-board inertial measurement unit. Uncertainties were at most 0.274 ± 0.008 for lift coefficient and 0.151 ± 0.005 for drag coefficient across all attitudes tested. The fins were also angled to allow the model to roll in free-flight so that roll coefficient could also be determined with a maximum experimental uncertainty of 0.411 ± 0.045.

Nomenclature

c = reference length (m)
δ_e = control surface deflection (°)
m = mass (kg)
p = roll rate (body axis) (rad.s^{-1})
q = pitch rate (body axis) (rad.s^{-1})
$\overline{q}$ = dynamic pressure (Pa)
r = yaw rate (body axis) (rad.s^{-1})
v = velocity perturbation (ms^{-1})

---

*D.Phil. Candidate, Department of Engineering Science;
†Senior Research Associate, Department of Engineering Science
‡Professor, Department of Engineering Science; matthew.mcgilvray@eng.ox.ac.uk

x, y, z = displacement (m)

$\ddot{x}, \ddot{y}, \ddot{z}$ = acceleration (m.s^{-2})

C_D = drag coefficient

C_L = lift coefficient

C_l = roll coefficient

C_M = pitching moment coefficient

I = moment of inertia (kg.m^2)

S = reference area (m^2)

θ = pitch angle (Euler) (°)

μ = dynamic viscosity (Pa.s)

ρ = density (kg.m^{-3})

ϕ = roll angle (Euler) (°)

ψ = yaw angle (Euler) (°)

V = freestream velocity (ms^{-1})

I. Introduction

Methodologies that can obtain high quality force and moment measurements in hypersonic facilities for complex sub-scale models remain important for the development of flight vehicles. The optimal method of testing a geometry is to undergo a flight testing programme, but this is very expensive, so ground testing and computational fluid dynamics are often used to optimise the design before proceeding to this stage. However, full nose-to-tail computational simulations still have limitations when predicting forces as there are large uncertainties in the prediction of phenomena such as boundary layer transition for example [1] [2]. Therefore, there is still need for ground-based experiments to act as a validation to these simulations.

Force and moment measurements in many hypersonic facilities that produce flight representative flow conditions is difficult due to the short time durations they produce, ranging from milliseconds in shock facilities to tens of milliseconds in Ludwieg tubes. Due to the short time scales, conventional methods of measuring forces such as using a statically calibrated strain-gauge sting-mounted force balance is not the optimal method for flow durations of less than 100 ms [3] and other force measurement techniques can be used which result in lower experimental uncertainties. It is challenging to design a model that can sufficiently damp out the internal stress waves produced by the external aerodynamic forces within these short test times to provide steady, equilibrium force measurements. To overcome this, the stress-wave force measurement technique was designed and implemented by Sanderson and Simmons [4] and more recently applied by Mee et al. [5] and Doherty et al. [6] which uses a carefully calibrated impulse response to deconvolve the forces from the measured strain signals. Whilst shown to be successful in short duration facilities with tests times of 1 ms, it requires careful design of the mounting structure so that it does not interact with the flow field and influence the measured forces [7].

To overcome sting interference and mounting vibrational effects, the free-flight force measurement technique was created [8]. Rather than mounting the model rigidly, the model is released into the facility nozzle core flow and allowed to move unconstrained in six degrees-of-freedom. This requires the kinematics of the model to be measured, usually by optical methods or on-board inertial measurement units (IMU). Free-flight wind tunnel experiments are discussed at length in Dayman Jr [9] and later in Bernstein and Pankhurst [8]. These very early efforts were limited by the lack of sophisticated technology at that time such as achieving high frame rate images or the availability of miniature-electronics. With the miniaturisation of IMU's driven by mobile phone technology, and the availability of high-resolution cameras with high frame-rates, there has been a strong resurgence of the technique over the last decade and it is now widely used in short-duration facilities around the world including for multi-body separation and space debris problems [10–15] and the measurement of static aerodynamic force coefficients of high-inertia models in shock tunnels [16–18]. Low inertia models in free-flight have also been used to measure aerodynamic forces as demonstrated by Mudford et al. [19] for a hemispherical-nosed cylinder, Kennell et al. [20, 21] with ESA's HEXAFLY INT EFTV geometry, McQuellin et al. [22] with an axisymmetric flyer and sustainer, and Hyslop et al. [23] for Reaction Engines' Skylon spaceplane. Due to the large degree of pitching motion of the model, the influence of dynamic derivatives is present which prompted the creation of the static free-flight technique [24]. For these experiments, the amount of pitching of the model was limited by matching the location of the centre of pressure and gravity, minimising the static margin to obtain purely static coefficients. This technique also produced uncertainties in aerodynamic coefficients below 3 %.

The static free-flight technique has been validated for simple geometries [24] with significantly smaller uncertainties than other force measurement techniques in the University of Oxford HDT [25]. Following the groundwork of previous experiments, the static free-flight technique is applied to a complex geometry in this work at conditions representative of a true flight vehicle. Complications exist with more complex geometries as the centre of pressure is unlikely to remain constant with angle of attack and so careful adjustments to the ballasting between experiments is required to match the centre of gravity to this location. The model used for these experiments is a 7 degree half-angle cone with 4 fins mounted at the base. As well as the measurement of longitudinal force and moment coefficients measured from image tracking and IMU measurements, the fins were angled and the model allowed to roll so that roll moment coefficients could be measured.

II. Static Free-Flight Technique

A. Aerodynamic Coefficients

The instantaneous aerodynamic coefficients in flight are summations of both static (time independent) and dynamic (time dependent) phenomena. Writing the aerodynamic coefficients in terms of their derivatives in three degrees of freedom motion, gives the following (higher order terms have been neglected):

$$C_X = C_{X_0} + C_{X_\alpha}\alpha + C_{X_{\delta_e}}\delta_e + C_{X_v}\frac{v}{V} + C_{X_q}\frac{qc}{2V} + C_{X_{\dot\alpha}}\frac{\dot\alpha c}{2V} + ... \tag{1}$$

Where:

$$C_{X_\alpha} = \frac{\partial C_X}{\partial \alpha}, C_{X_\delta} = \frac{\partial C_X}{\partial \delta}, C_{X_v} = \frac{\partial C_X}{\partial (v/V)}, C_{X_q} = \frac{\partial C_X}{\partial (qc/2V)}, C_{X_{\dot\alpha}} = \frac{\partial C_X}{\partial (\dot\alpha c/2V)} \tag{2}$$

Where X is either lift, drag or pitching moment. To measure purely static derivatives in wind tunnel facilities, the experimenter must remove the ability of the model to exhibit any dynamic behaviour with time. From equation 1, it can be seen that to remove any dynamic influence on the coefficients, two criteria must be fulfilled; the model must not be allowed to pitch and there must be minimal perturbations in the freestream velocity. The dependency on flow perturbations (or gusts in flight), C_{X_v}, can be assumed to be minimal in wind tunnel facility which generates constant freestream conditions and have small perturbations in the free-stream velocity during the test time. If the model is not allowed to pitch during the test and the angularity changes to the flow are uniform with respect to model position, the effects of C_{X_q} and $C_{X_{\dot\alpha}}$ may be negated. By fulfilling these conditions, a purely static condition is achieved and only the static coefficients are measured. This reduces Eq. 1 to:

$$C_L = C_{L_0} + C_{L_\alpha}\alpha + C_{L_{\delta_e}}\delta_e \tag{3}$$

For aerodynamic coefficients measured in wind tunnel facilities to be representative of those in flight, the conditions must be scaled so that similitude is achieved. Aerodynamic coefficients are functions of both Mach number and Reynolds number, with Mach number similitude preserving compressibility effects (such as shock angles) and Reynolds number similitude preserving viscous effects (such as boundary layer thickness and skin friction). Therefore, matching both of these dimensionless groups and limiting the ability of the model to pitch allows for static aerodynamic coefficients to be measured.

B. Methodology of Static Free-Flight

For free-flight testing, the scaled model is free to move in six degrees of freedom so it is not possible to constrain the model from pitching through the use of rigid mounts to remove the influence of dynamic phenomena during a test. In free-flight, there are two ways of preventing pitching motion; the first is to have a model with sufficiently high inertia that during the test time the resultant pitching is minimal. This would likely result in a large, heavy model. Increasing the model's mass decreases the magnitude of the accelerations which would occur during the test, making it harder to measure the forces and increasing the uncertainty of the experiment.

The second method of minimising the pitching, which was used in these experiments, is to manipulate the aerodynamic pitching moment that acts on the body during the free-flight test. Consider the aerodynamic forces acting on a free body in free-flight; as the fluid passes over the body during a test, pressure and shear components are exerted on the surface of the body. Integrating the shear and pressure components over the body results in the overall aerodynamic force acting on the body. This integrated force can be considered to be a single force vector at the average integrated location, often referred to as the centre of pressure (CoP). The force vector is usually split into two orthogonal forces referred to as lift and drag. The final force that needs to be considered is the model's weight which can be considered to act as a single vector through the centre of gravity (CoG). The position of the CoG relative to the CoP determines the stability of the body in flight. If the CoG is fore of the CoP, the body is statically stable and will tend to pitch towards an equilibrium position if perturbed. If the CoG is aft of the CoP, the body is statically unstable and will pitch away from an equilibrium position which is often undesirable as it makes the body difficult to control. In both of these instances, the body will exhibit increasing pitch rates as the distance between the CoP and CoG is increased. If a model is designed so that the CoP is at the same position of the CoG, there will be no aerodynamic pitching moment and hence can be considered as a static free-flight test.

In practice, this requires: (1) a method of predicting the CoP location, (2) a model design that allows for fine tuning of the CoG location and (3) a setup that can accurately measure the CoG location before a test. It should be noted that in this static free-flight methodology, the model design is independent of mass and moment of inertia and so the experimenter is not limited by material choice as they would be if scaling for dynamic experiments which require strict similitude criteria to be matched for mass and inertia to obtain flight representative dynamic derivatives.

III. Experimental Setup

A. Facility and Freestream Conditions

The free-flight experiments were conducted in the University of Oxford High Density Tunnel HDT, a heated Ludwieg tube that provides cold, high Reynolds number flow for steady plateaus of approximately 50 ms. The facility is rated for fill pressures of up to 275 bar which during a test is vented from a barrel through a quick-acting plug valve to a contoured converging/diverging nozzle with exit diameter of 350 mm. This provides a core flow of 280 mm at nozzle exit. The nozzles can be changed to provide a freestream Mach number of integers between 5 and 7. For further details on the HDT operation and measurement of freestream conditions, see McGilvray et al. [26] and Wylie et al. [27].

Figure 1 shows a schematic of the Oxford HDT.

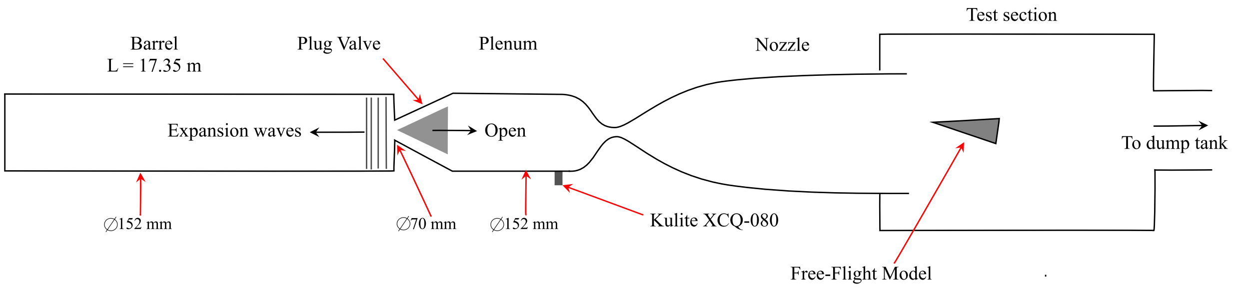

Fig. 1 Schematic of the University of Oxford HDT

The freestream conditions used for the experiments were representative of a flight vehicle at an altitude of 35 km and Mach number of 7 [28]. To scale for these conditions, Reynolds and Mach number were matched between flight and tunnel, and it was assumed that full scale vehicle was 3 m in length, giving a scale factor of 1/12 for a 250 mm length wind tunnel model. This provided a model which is suitably sized for the core flow of the facility. The tunnel and flight freestream conditions are shown in Table 1 below.

Table 1 Mach 7 Flight vs scaled tunnel condition.

Measured Freestream Properties	**HDT Test Flow**	**Flight**
Total Pressure (kPa)	3348 ± 7	2313
Pitot Pressure (kPa)	49.9 ± 0.7	35.5
Total Temperature (K)	555 ± 15	2560
Calculated Freestream Properties		
Altitude (km)	35	35
Mach Number	7.05 ± 0.02	7
Velocity (ms^{-1})	1006 ± 14	2160
Density (kgm^{-3})	0.0532 ± 0.0018	0.0082
Static Pressure (Pa)	774 ± 15	559
Static Temperature (K)	50.8 ± 1.4	242
Dynamic Viscosity (μPas)	3.64 ± 0.10	15.2
Dynamic Pressure (kPa)	26.9 ± 0.6	19.1
Unit Reynolds Number ($10^6 m^{-1}$)	14.7 ± 0.7	1.16
Reynolds Number (10^6)	3.68 ± 0.16	3.48

The conditions obtained during a test were surveyed prior to the experiments using a rake instrumented with pressure transducers and thermocouples, providing freestream total pressure, Pitot pressure and total temperature traces. From these measurements, the Pitot-to-nozzle-supply ratio was used to calculate Mach number, Keyes' Law to calculate dynamic viscosity [29] and isentropic relations to calculate the rest of the tunnel conditions. Equivalent flight conditions were calculated through US Standard Atmosphere [30] and viscosity using Sutherland's Law [**?**]. The uniformity of the core flow with respect to axial position was also measured with the rake. The core flow was determined to be of 280 mm diameter at nozzle exit reducing to 240 mm at 300 mm downstream. Uncertainties in the calculated freestream variables are determined using the Taylor Series Method through the propagation of uncertainties from the measured properties. Computation fluid dynamic (CFD) simulations of the nozzle conducted in Eilmer4 show agreement with the measured core flow diameter at nozzle exit and predict the angularity of the flow to remain within +/- 0.12 ° within the core flow.

B. Test Infrastructure

The test infrastructure used to conduct free-flight experiments is shown in Figure 2 with the finned cone model in the test section prior to an experiment. The infrastructure can be split into three working functions; the release mechanism, protection of the model and optical setup aides. The infrastructure originates from Hyslop et al. [24] with some improvements.

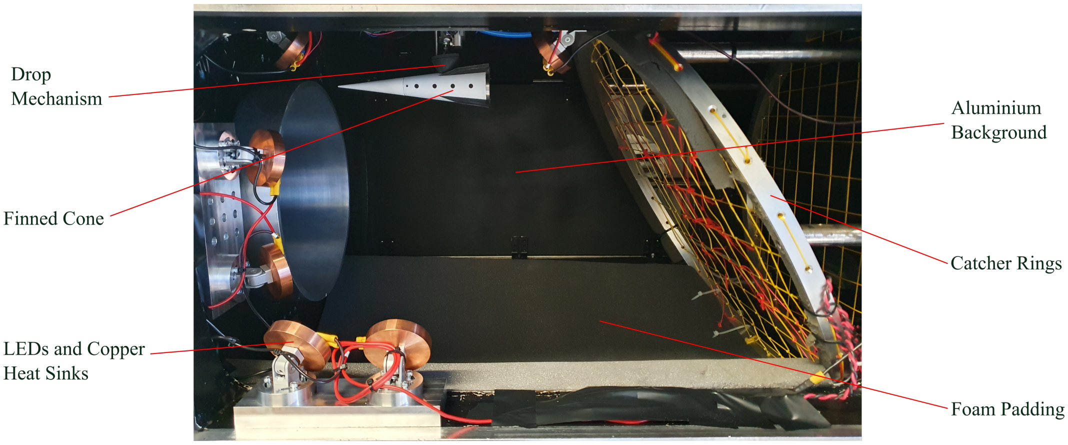

Fig. 2 Free-flight infrastructure in the HDT test section.

The drop mechanism is used to release the model so that it is in the centre of the core flow when the facility is fired. A 25 mm Eclipse Magnetics electromagnet is used to hold the model in place. Prior to the facility firing, a TTL trigger is sent to a bespoke electronics box which causes the electromagnet to release. This timing can be adjusted as the flow initiation is achieved by the motion of a fast-acting plug valve whose timings are well calibrated. The electronics box also activates two 100 psi solenoids that retract a 50 mm stroke length actuator. This removes the electromagnet from the core flow, preventing any shocks influencing the model during the test. The electromagnet is encased in a 3D printed holder which fits conformal to the shape of the finned cone model with different variations printed to set the angle of attack in two degree increments. A steel rod can be inserted into the holder which fixes the model position in yaw. The axial and roll location are fixed by painting a ’T’ shape to the model which the conformal holder is designed to locate. The drop mechanism is mounted to a linear rail so that its axial position relative to the nozzle exit can be adjusted.

The model is protected after a free-flight experiment by two aluminium catcher rings. The rings are designed to be strung similar to a tennis racket using Dyneema cord which has a high tensile yield strength. The upstream ring is angled at 30 ° to the vertical and is designed to deflect the model towards the floor of the test section on impact which is padded with triple layer density foam, providing a soft landing to protect the model. The second downstream ring lies parallel with the test section exit and provides a redundancy in case the first ring is breached to prevent the model entering the dump tank where it becomes difficult to retrieve.

Located within the tunnel were six Luminus PT-120-B-L11-EPG LEDs of 460 nm peak wavelength (blue light) with individual copper heat sinks. The position and rotation of these LEDs could be adjusted to provide sufficient and uniform lighting to the track the model at high frame-rates. This setup also allows for pressure-sensitive paint to be painted onto the model if required [31]. At the far side of the test section from the optical setup is a painted black aluminium paint which provides a high contrast, uniform background against the white model to allow for improved edge detection for the image tracking algorithm.

C. Experimental Model

The experimental model shown in Figure 3 is a 7 degree half-angle cone of 250 mm length with four fins attached to the base of the model at cardinal positions. The fins, shown in Figure 4, were designed so that they did not interact with the bow shock from the nose tip of the cone calculated from a Taylor-Maccoll analysis of Mach 7 flow at zero degrees angle of attack. This results in fins of width 15.7 mm at the base which taper for a length of 83.3 mm (a third of the length of the body). The leading edges of the fins are angled at 20 degrees to keep the flow attached with a bluntness of 0.2 mm radius for machining reasons. The fins could be angled at ±3° but for the main body of the work were set to 0°. The fins were 3D printed so that they could be easily manufactured and replaced in the event of damage after free-flight. For the experiments, the model was tested with the fins oriented at 45 ° to the horizontal.

The body of the cone was machined from steel and could be split into two halves. This allows for easy access when instrumenting the model with on-board sensors and ballast. The base was also machined from steel and had notches which allowed for the fins to be bolted into place, ensuring sufficient rigidity in mounting. The two halves of the cone join to form a male thread to which nose tips of different bluntnesses could be attached. For this work, a bluntness of 1.25 mm in radius was used. Internal to the model was an on-board DAQ which contained inertial measurement units. The DAQ was rigidly mounted to a 3D printed holder which was shaped to be conformal to the internal shape of the cone and remain fixed during a test. The external surface of the model was painted white to provide high contrast between the model and the black background of the test section to improve the accuracy of the edge tracking algorithm. After painting white, a laser cut stencil was used to paint black circles on the side of the cone and 'T' shapes at the top the cone with a positional tolerance of ± 0.2 mm.

An important aspect of static free-flight tests is that the centre of gravity (CoG) is in the same position as the centre of pressure (CoP) of the model. Prior to experiments, the COP was calculated using a panel method code with tangent cone pressure predictions to be 70.7 mm (from the base) at zero degrees angle of attack with a variation of ± 1 mm for

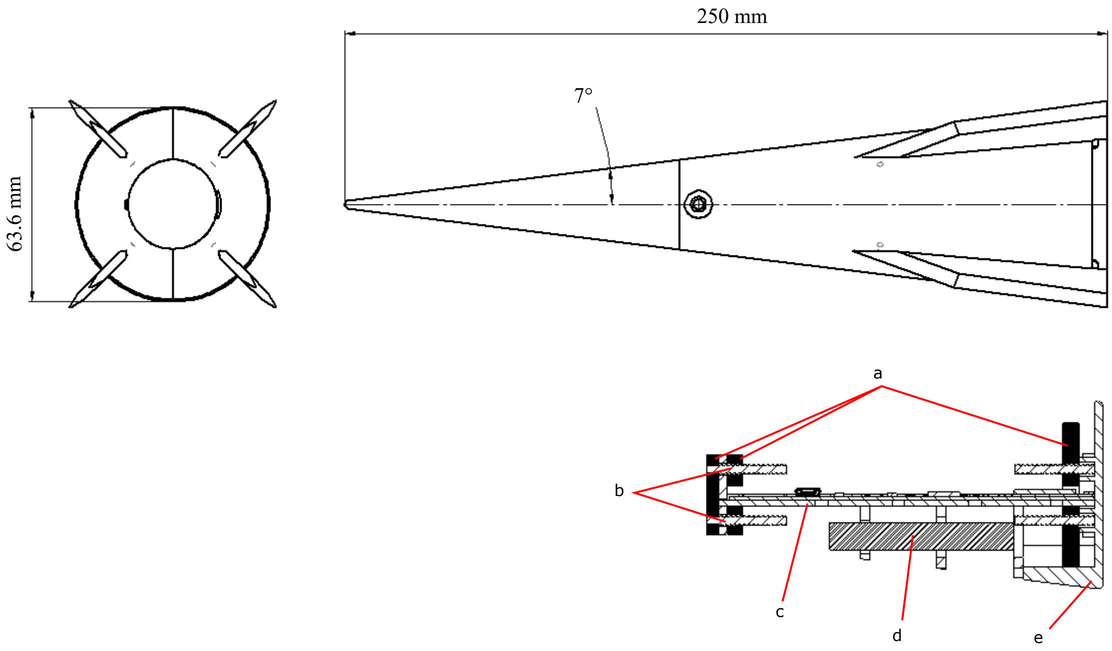

Fig. 3 Finned cone experimental model with major geometric dimensions. Bottom shows the schematic of the internal instrumentation support (a - Tungsten ballast, b - threaded rod, c - DAQ, d - battery, e - 3D printed mount)

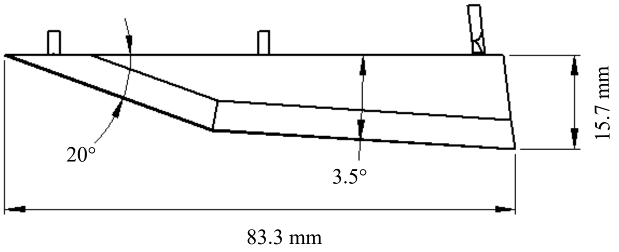

Fig. 4 Major dimensions of fin geometry used in this work

Table 2 Model inertial and geometric properties

Length (mm)	250 ± 0.2
Cone Half-Angle (°)	7 ± 0.03
Nominal Nose Radius (mm)	1.25 ± 0.1
Base Area (m^2)	3.2 x10^{-3} ± 0.01
Centre of gravity (mm)	70.7 ± 0.1
Mass (g)	832.323 ± 0.001
Pitching Moment of Inertia (kgm^2)	2.91 x10^{-3}
Roll Moment of Inertia (kgm^2)	0.30 x10^{-3}

the angles of attack of interest. To demonstrate the influence of static margin position and pitch rate, Figure 5 shows an analytical prediction of the rate the finned model would pitch from 6 ° angle of attack with various static margins (difference between CoP and CoG) using the inertial properties in Table 2, the freestream conditions in Table 1 and aerodynamic coefficients from a panel method code. It is presented over 50 ms as this represents the test time of the HDT. It can be seen that a mismatch in CoG location to CoP of 1 mm can cause the model to pitch by over a degree in the test time. Therefore a lot of care must be token when ballasting the model and the CoG position must be changed between experiments if the angle of attack is changed if static free-flight is to be achieved with small changes of angle of attack over the test time (less than ± 0.5 °).

The model was designed to feature ballasting which could place the CoG in this predicted location and the ability to adjust for experimental corrections. To achieve this, tungsten ballast could be placed at both the front and rear of the cone internal section and was adjustable using threaded rods and nuts. The ballasting tungsten can be seen in Figure 3 shaded black. The centre of gravity was measured using a moment balance, whereby the model was suspended using two strings. The tension in the upstream string was measured using a load cell. This setup allowed the CoG to be determined to +/- 0.1 mm. The inertial properties of the model are shown in Table 2.

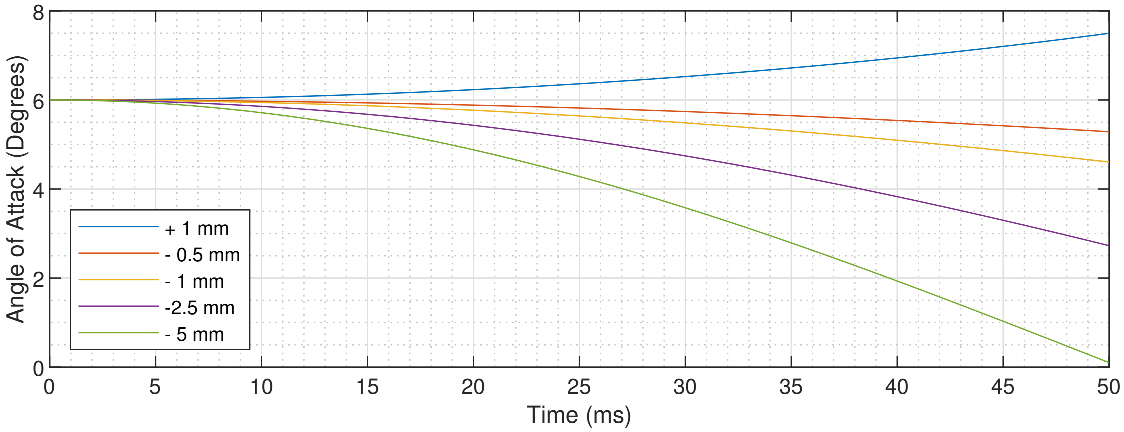

Fig. 5 The influence of static margin on pitch as predicted by an analytical model for the finned cone model

D. On-Board Data Acquisitions

The on-board inertial measurement board were designed and built by UNSW Canberra [32]. The board consisted of an integrated 3-axis accelerometer and 3-axis gyroscope, non-volatile memory, a Bluetooth radio module and a microcontroller, all integrated on a single printed circuit board of dimensions 114 mm x 12 mm. The IMU was a single chip containing both the accelerometer and gyroscope. The accelerometer had a full scale range of +/- 16 g and a data output rate of 4 kHz whilst the full scale range of the gyroscope was +/-2000 deg/s with a data output rate of 8 kHz. The board could be armed prior to testing to be triggered by the detection of sustained free-fall of the model release. A sampling rate of 8 kHz was used for this work which allowed for 320 samples to be obtained over the 40 ms of test time in free-flight. Non-linearity of the accelerometer and gyroscope axis is reported to be 0.1% and 0.5% respectively.

E. Optical Setup

The optical setup was designed to allow for longitudinal imaging of the model during free-flight at high frame rates to measure the model's linear and angular displacements. The camera was a monochrome Phantom TMX 7510 which allows imaging of uncropped frame rates of up to 76,000 fps at a resolution of 1 Mpx. The lens mounted to the camera was a Tamron 24-70mm f2.8 lens set to a focal length of 50 mm and aperture of f2.8. The camera was positioned to face perpendicular to the longitudinal plane of motion so that the full test section was visible during a test. The camera was aligned with the test section using two plumblines suspended from known points on the test section. To allow for the images to be sufficiently exposed at 76,00 fps, six Luminus PT-120-B-L11-EPG LEDs were used to illuminate the test section, providing uniform lighting over the entire test area.

IV. Data Processing

Forces and moments are presented in aerodynamic coefficient form, defined by the force or moment non-dimensionalised by the freestream dynamic pressure (Table 1) and a reference area (Table 2), plus an additional reference length (the length of the model) for moment coefficients. In free-flight, these equations can be written as follows:

$$C_L = \frac{m\ddot{z}}{\overline{q}S}, \quad C_D = \frac{m\ddot{x}}{\overline{q}S}, \quad C_M = \frac{I_{yy}\ddot{\theta}}{\overline{q}Sc} \tag{4}$$

For these experiments, forces are derived using two independent methods. One method is image tracking and the second is through on-board accelerometers and gyroscopes. The data reduction is discussed in more detail for both methodologies in this section.

A. Inertial Measurement Unit

Accelerometers and gyroscopes provide direct information on the accelerations and angular rates acting on a body. The complexity in the processing of the measured data lies in transforming frames of reference from the body's reference to the Global frame of reference. The Body frame of reference is defined relative to the model as +x towards the nose of the vehicle, +z towards the bottom of the vehicle with +y completing the orthogonal system. This is the frame of reference in which the IMU board is moving within. The Global or Earth frame of reference is defined as having the +z axis towards the ground, +x axis pointing upstream towards the facility nozzle and the +y axis orthogonal to both to form a right-hand coordinate system. This frame of reference is what all global force coefficients are defined relative to. Figure 6 shows a graphic of the co-ordinate systems overlaid on the finned cone model.

As the Body frame of reference in free-flight is constantly changing with respect to the Global frame of reference, transformations are required to turn the measured body accelerations into global accelerations and hence forces. To transform the data, first the body angular rates are transformed to Euler angular rates using Eq. 5, allowing the Euler

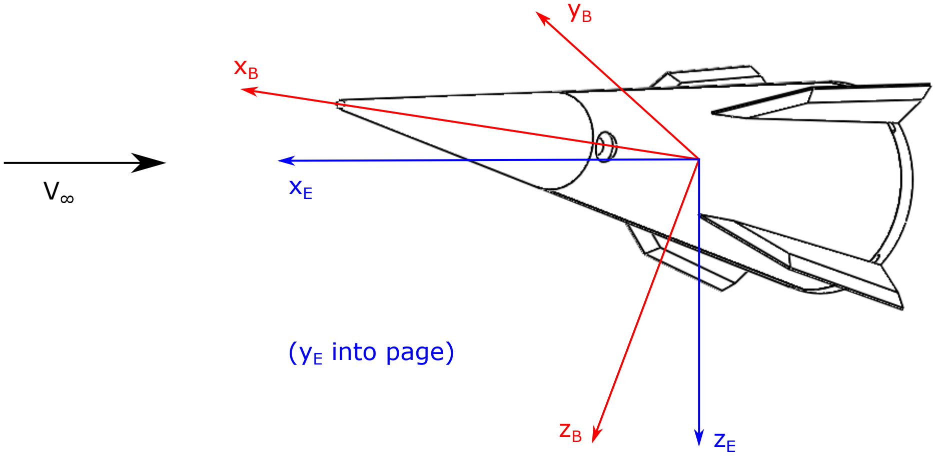

Fig. 6 Earth and body co-ordinate systems overlaid on finned cone

angles to be determined via numerical integration of Euler-rates. Knowledge of the Euler angles allows for the linear accelerations as measured by the IMU to be transformed to the Global frame of reference according to Eq. 6. The raw IMU measured accelerations are filtered with a 6th order low pass Butterworth filter with a cut of frequency of 500 Hz to remove high frequency noise prior to undergoing the transformations. Finally the aerodynamic coefficients can be obtained using Eq. 4 and averaging the accelerations over the test time.

The rotation matrix for the angular rates and accelerations (subscript E for Earth coordinates and B for body coordinates) are as follows (where c, s and t are cosine, sine and tangent functions respectively, p, q and r are body roll, pitch and yaw rates respectively and ϕ, θ and ψ are Euler angles):

$$\begin{bmatrix} \dot{\phi} \\ \dot{\theta} \\ \dot{\psi} \end{bmatrix} = \begin{bmatrix} 1 & s(\phi)t(\theta) & c(\phi)t(\theta) \\ 0 & c(\phi) & -s(\phi) \\ 0 & \frac{s(\phi)}{c(\theta)} & \frac{c(\phi)}{c(\theta)} \end{bmatrix} \begin{bmatrix} p \\ q \\ r \end{bmatrix} \tag{5}$$

$$\begin{bmatrix} \ddot{X} \\ \ddot{Y} \\ \ddot{Z} \end{bmatrix}_E = \begin{bmatrix} c(\psi)c(\theta) & c(\psi)s(\phi)s(\theta) - c(\phi)s(\psi) & s(\phi)s(\psi) + c(\phi)c(\psi)s(\theta) \\ c(\theta)s(\psi) & c(\phi)c(\psi) + s(\phi)s(\psi)s(\theta) & c(\phi)s(\psi)s(\theta) - c(\psi)s(\phi) \\ -s(\theta) & c(\theta)s(\phi) & c(\phi)c(\theta) \end{bmatrix} \begin{bmatrix} \ddot{X} \\ \ddot{Y} \\ \ddot{Z} \end{bmatrix}_B \tag{6}$$

Figure 7 shows a typical trace of the measured filtered linear accelerations for a test with the finned cone at -4 ° angle of attack. As seen in the figure, the model free-falls for approximately 130 ms before the onset of flow. During this time the model falls into the centre of the core flow of the tunnel. The tunnel takes 35 ms to start up before the steady plateau in freestream conditions are reached. It is during this steady plateau that the test time is taken. The filtered accelerations in the direction of lift and drag mimic the plateau in free stream stagnation pressure. The accelerations stay constant during the steady test time due to the minimal pitching exhibited by the model during a test. It can be seen, however, that there is a non negligible out of plane acceleration suggesting the model was initially slightly yawed with respect to the facility centre-line. With the current experimental setup and optical access, it is not easy to precisely align the model in yaw with the flow freestream. This acceleration will cause the measured drag coefficient to be slightly increased.

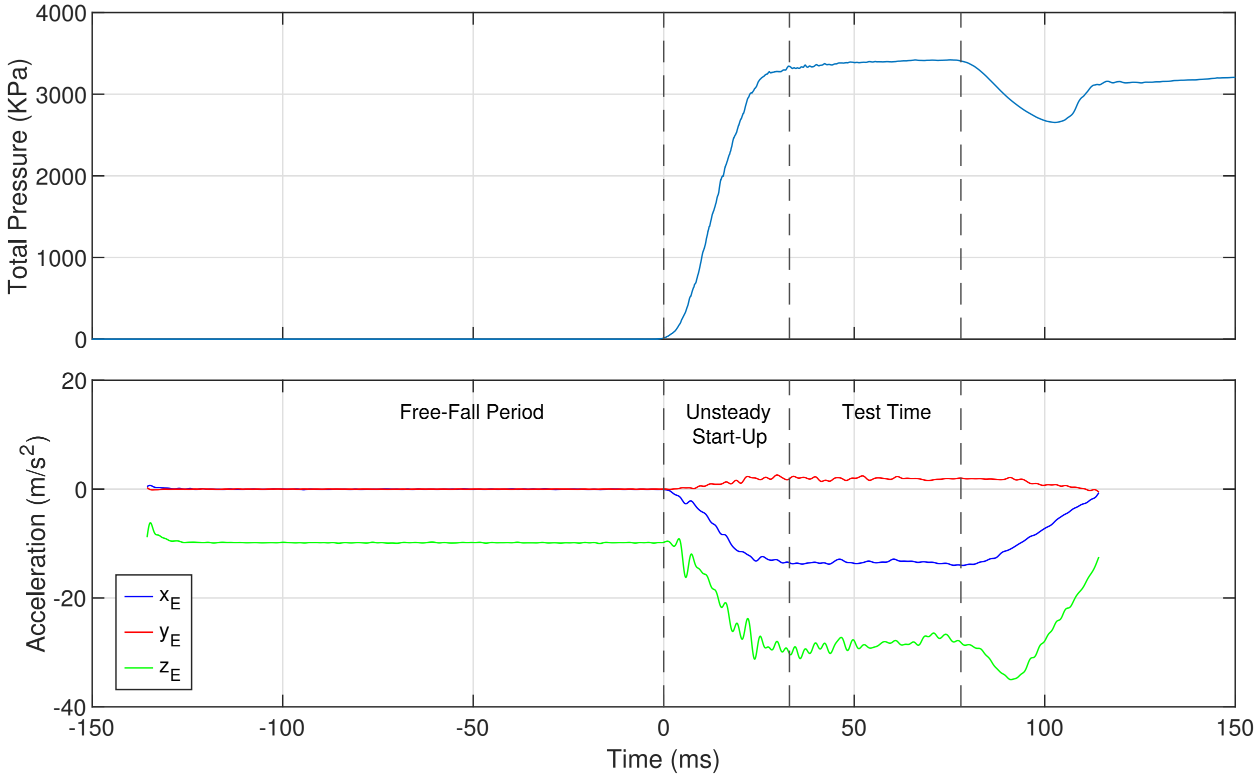

Fig. 7 Linear accelerations as measured by the IMU with freestream total pressure. The finned cone is at - 4 ° angle of attack for this test.

B. Optical Tracking

The second methodology used to obtain force coefficients in free flight is through optical tracking. Rather than directly measuring accelerations, optical tracking measures the model's displacement and angle of attack history and therefore requires double differentiation of the displacement data to obtain accelerations. It is highly desirable that the tracking data is as smooth and noise free as the differentiation process amplifies any noise in the data.

The algorithm used in this work is the same as used in Hyslop et al. [24]. It works by detecting the centre point of two circles of known position on the model. From these two centre points, the centre of gravity can be determined as the location is measured before an experiment. Detecting the centre of gravity for each frame gives a displacement history of the model in free-flight. For longitudinal tracking of the finned cone in free-flight (about pitch axis), four accurately located black circles are painted on the side of the model. Only two circles are required by the algorithm; the additional two circles are added for redundancy in the case of damage or non-uniform lighting. The methodology for image tracking is briefly summarised as follows:

1) Apply Gaussian filter to image and subtract from original (High pass filter).
2) Apply Canny filter to image so that only pixels detected as an edge are shown [33].
3) Apply Hough transform to find circles in the image after narrowing the search radius [34].
4) Detect pixels in the proximity of the circle located by the Hough transform.
5) Use sub-pixel detection on the original image using the methodology set out in von Gioi and Randall [35] at the location where pixels were detected by the Hough transform.
6) Fit a circle to the pixels using linear regression as set out in Laurence et al. [36] and use this equation to find the centre point of the circle.

After detecting the location of the two circles, a line is fitted between them for which the position of centre of gravity lies on. The distance of the centre of gravity is known relative to the circles and this process is repeated for each frame giving a time history of centre of gravity displacement. The physical distance between the two circles is also used as a reference to scale the image from pixels to metres. For the setup in this work, the scaling factor was 0.68 mm/pixel. Shown in Figure 8 is the image tracking algorithm overlaid on an example finned cone free-flight test. The red line indicates the location of the centre of gravity during the test time as detected and can be seen to remain in the core flow for the duration of the test time. Prior to testing, the spatial uniformity of the lens was measured and corrected for through the use of a uniform grid inserted into the tunnel using the Matlab camera calibrator algorithm.

To determine the aerodynamics coefficients, the displacement data is differentiated twice to give the accelerations and hence aerodynamic coefficients using Eq. 4. The intermediate velocity was numerically smoothed using a Gaussian filter before being differentiated into accelerations. The maximum filter window for this process corresponds to 15 ms which is sufficiently less than the facility test time (40 ms) and allows steady aerodynamic forces to be determined as the static free-fight methodology reduces the pitching of the model, resulting in near constant forces. The forces and

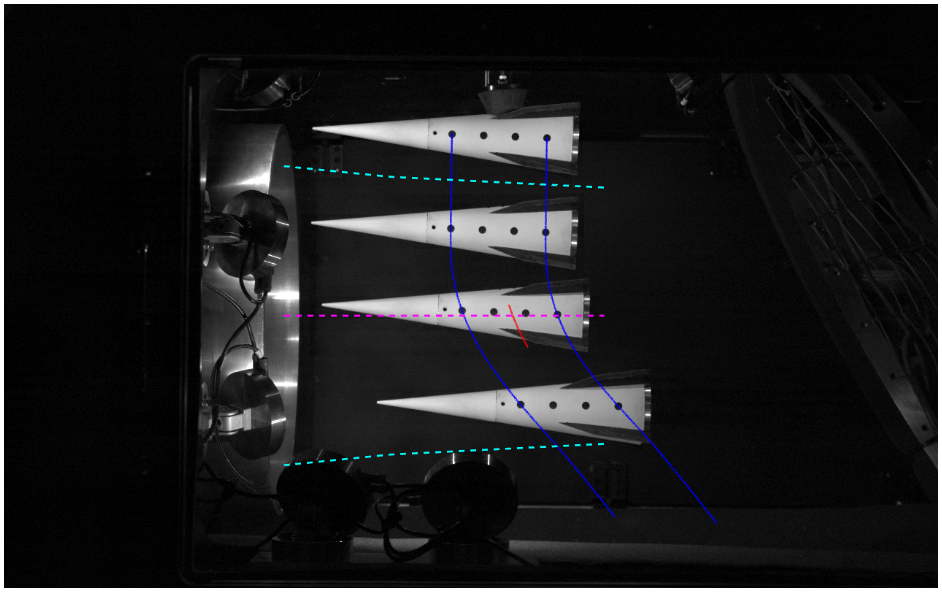

Fig. 8 Montage photo of image processing (Blue - detected circle centre points, Red - calculated centre of gravity, shown for test time, cyan - core flow location as acquired by a pitot survey, pink - nozzle centreline).

moments are then averaged over the test time to then calculate the aerodynamic coefficients.

Angle of attack was determined using the edge of the cone and finding the relative angle to the horizontal. The edge is detected through the use of a Canny filter followed by sub-pixel detection to find the true edge. The model edge is the preferred method of detecting angle of attack (over the circles) as it is unaffected by model roll for axisymmetric geometries. Painting the model white gave strong contrast between the black background and the edge of the model.

The accuracy of the image tracking algorithm was calculated to be ± 4 μm in Hyslop et al. [24] which is small considering the pixel resolution was 0.68 mm/pixel. The accuracy in angle of attack using the same methodology was determined to be ± 0.01 °. This analysis, however, did not take into account errors which result from misalignment of the optical equipment but gives an approximation of the uncertainty associated with the numerical algorithm.

C. Freestream Alignment

The alignment between the tunnel freestream and model for sting mounted model is often corrected through the use of four radial pressure transducers which show that the model is aligned when all read the same value. In the current free-flight setup, there are no pressure transducers so the angle relative to the freestream is unknown. To resolve this issue, an alignment probe (four radial pressure transducers, north, east, south and west) was sting mounted to a two axis traverse and experiments were conducted to find the true zero angle of attack. This is at the point where the north and south pressure transducer read the same static pressure value. The optical cameras were used to calculate the angle of attack from their reference point and this offset was subsequently applied to all of the experimental data. The offset in angle of attack at Mach 7 was found to be +0.4 ± 0.05 ° for this test campaign and was used as the 0 ° reference for all experiments. The camera set up remained fixed between free-flight tests and alignment test. In an ideal setup with sufficient optical access, this process would also be conducted on the yaw plane too to guarantee full alignment with the freestream.

D. Comparison of IMU and Image Tracking

Figure 9 compares the image tracking and IMU results for the model kinematics for a single free-flight test at -4 ° angle of attack. The image tracking measures displacements directly so the accelerations are determined from differentiation and the IMU measures accelerations directly so the displacements are determined through integration. Figure 9 shows a comparison of the kinematics of the finned cone model for the image tracking and IMU in a single tests. The agreement between the two methodologies demonstrates that either method can reliably be used to accurately measure static aerodynamic coefficients in free-flight experiments.

For both the horizontal and vertical acceleration, the agreement between the two independent methods is within 5 % during the test time. Importantly, the vertical acceleration during free-fall agree and measures at the value of gravitational acceleration in a vacuum. The IMU shows small vibrations superimposed on the signals which is the result of internal vibrations passing through the internal mounting structure that supports the IMU during the free-flight test. The agreement between the velocity and displacement data on both axes is also good for the entire duration of the experiment, with a slight deviation in the horizontal displacement over the test time/colorblack. The trace for angle of attack appears to have less agreement between the data sets but the discrepancy between the two measurements remains within ± 0.1 ° during the experiment which is considered acceptable. This difference is expected to be a consequence of only optically tracking the model in 3 degrees of freedom - for this model small changes in yaw affect the detected pitch angle. It can also be seen in the 130 ms free-fall period, the model only pitches 0.15 °.

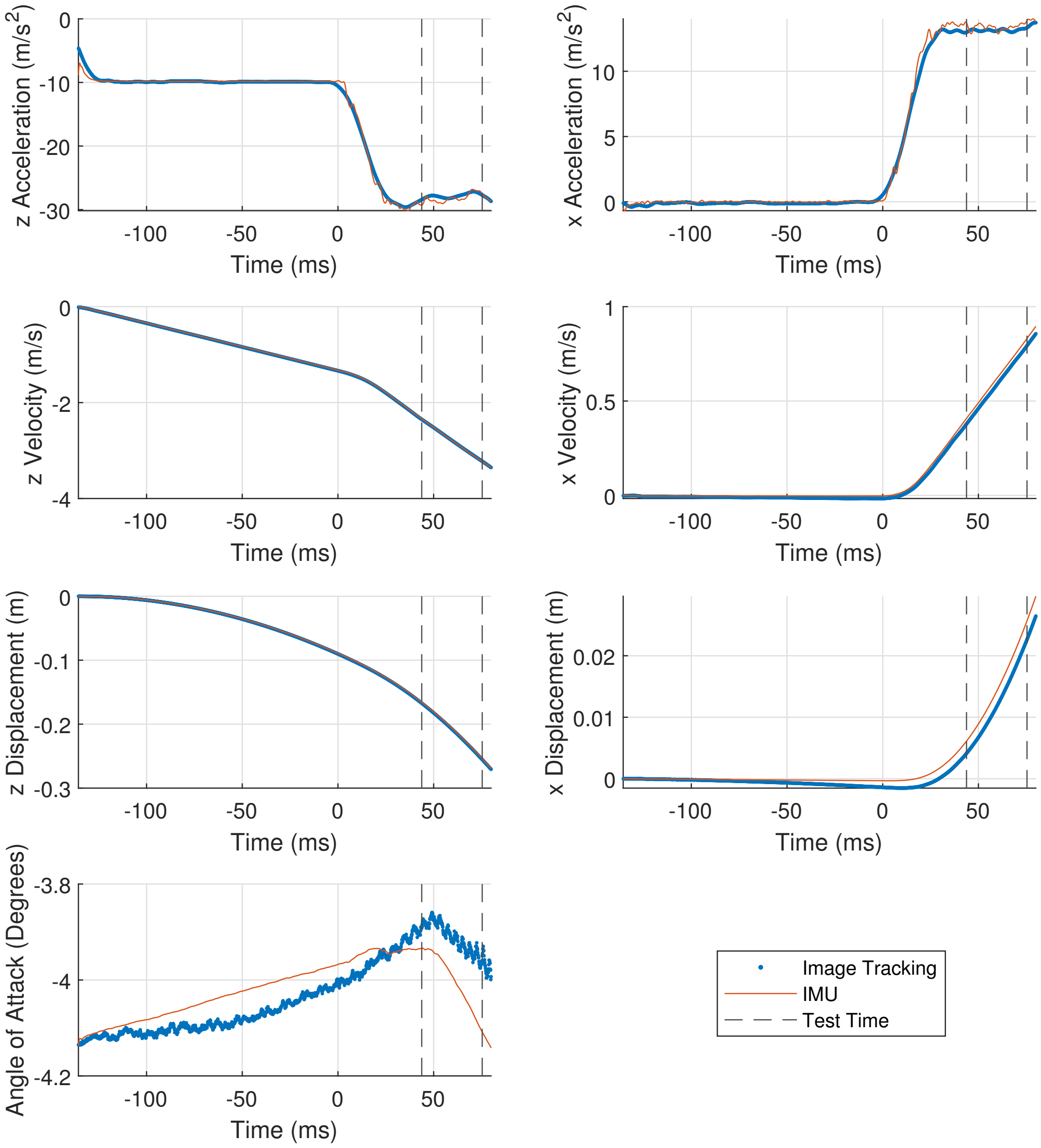

Fig. 9 Comparison of longitudinal motion as measured by image tracking and IMU data. Time = 0 is the point of flow initiation.

V. Experimental Results

This section presents the results from the free-flight experiments with the finned cone. In total 14 experiments were conducted ranging between -6 ° and 6 ° angle of attack so the half-angle of the cone was never exceeded. Lift, drag and pitching moment data are shown, as well as centre of pressure variation at the Mach 7 conditions. The experimental results are shown for both the IMU data and optical tracking and presented against viscous tangent cone predictions from a numerical panel method simulations [24]. Uncertainties are shown as error bands around the data points as calculated using the Moffat's error propagation method [37] for freestream parameters, model properties, IMU and image tracking.

To produce numerical predictions of the finned cone in free-flight, a panel method code was utilised. This code utilised a tangent-cone method to calculate the pressures over the slender body of the cone. If the surface becomes sufficiently blunt, i.e over the nose of the cone, Modified-Newtonian predictions are used in these regions. For the fins, the post conical shock pressures combined with shock-expansion calculations over the fin geometry were used to calculate the pressures in this region. For more details of the panel method code, see Hyslop et al. [24]. For the subsequent plots, both the predictions for a cone with no fins and fins are presented.

A. Aerodynamic Coefficients

Figure 10 presents the measured variation in lift coefficient with angle-of-attack and a comparison with viscous tangent-cone calculations. It can be seen that the trend is generally linear and as expected, more lift is generated than for the cone without fins. The numerical prediction slightly over predicts the aerodynamic coefficients at the extremities but the general trend is in good agreement. The lift coefficient is zero at 0 ° angle of attack which is expected for a body with symmetry about the yaw plane.

Drag coefficient variation with angle of attack is shown in Figure 11. The experimental data agrees well with the viscous numerical prediction and exhibits the expected parabolic shape. The fins increase the drag compared to the model with no fins as the frontal area of the cone is increased. It can be seen in the figure that at high angles of attack that the agreement between the drag coefficient for the IMU and image tracking gets worse (although remaining within experimental uncertainty). At high angles of attack, the cone was more likely to exhibit a small amount of roll. This resulted in measurement artefacts where the small angular roll would superimpose onto the translational motion measured by the image tracking algorithm, influencing the measured displacements and hence forces. As measured by the IMU for the high angle of attack tests, the model was exhibiting a slight clockwise roll at positive angles of attack. This influence could be removed by tracking the boundary of the model rather than using dots.

Figure 12 shows the variation of the lift-to-drag ratio with angle of attack. The overall agreement with the numerical prediction is good. The graph shows that the lift-to-drag ratio for a cone without fins is the same as for the cone with fins. This shows that adding extra control with fins does not sacrifice this parameter.

Figure 13 shows the variation of pitching moment against angle of attack as referenced from the nose of the cone. From this location, the gradient is negative showing that the vehicle is statically stable with the centre of gravity at this location, as expected. Furthermore, the trim angle of attack is 0 ° which again is expected for this geometry. Figure 14 shows the variation of centre of pressure with angle of attack. Unlike for a cone with no fins, the numerical simulation predicts the centre of pressure to move with angle of attack by ± 0.7 mm within the tested range of angles of attack. If the CoG was kept in a constant position for all angles of attack, the change in static margin due to the shift in CoP can

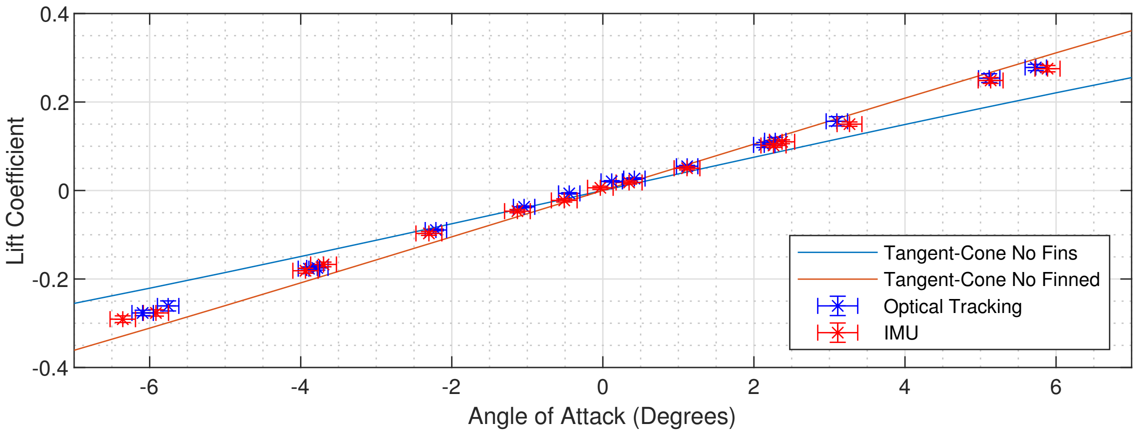

Fig. 10 **Lift coefficient at Mach 7 condition. Individual tests plotted against tangent-cone numerical prediction**

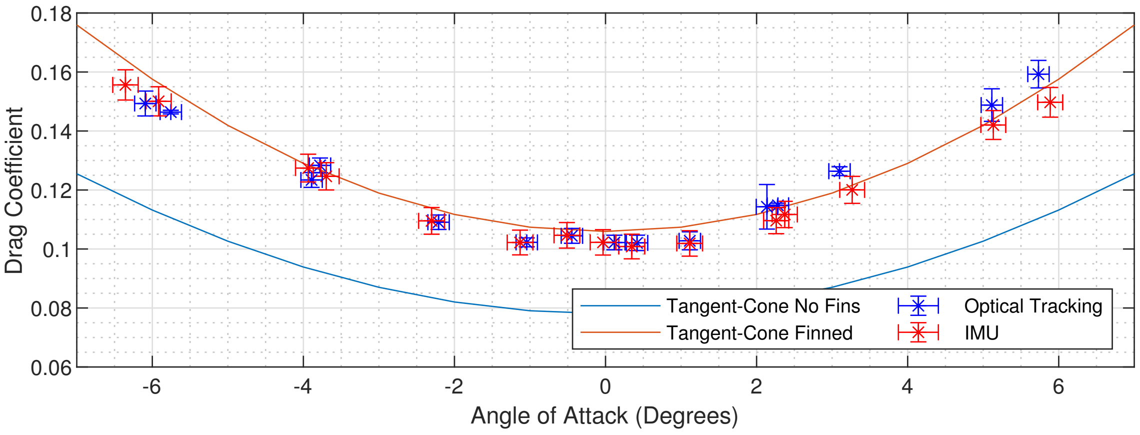

Fig. 11 **Drag coefficient at Mach 7 condition. Individual tests plotted against tangent-cone numerical prediction**

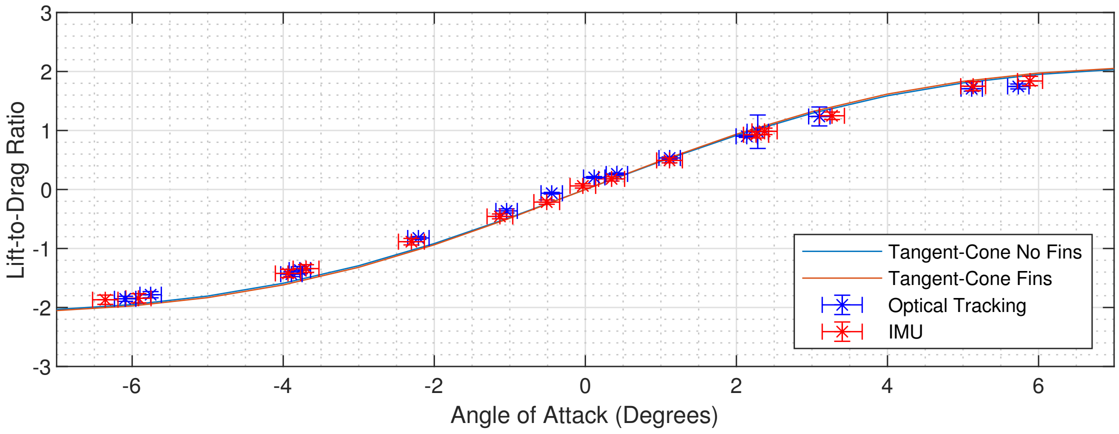

Fig. 12 **Lift-to-drag ratio at Mach 7 condition. Individual tests plotted against tangent-cone numerical prediction**

cause the vehicle to pitch more during a test making the static free-flight methodology more difficult to achieve. As a result, more shots are required when changing angle of attack to adjust the ballast of the model to be in the correct location so that the pitch remains at less than half a degree in the test time. The large measurement uncertainties in

CoP are a result of having the CoG close to the CoP. As the measured pitching moment (about the centre of gravity) is small/negligible, it leads to large uncertainties in the derivation of CoP.

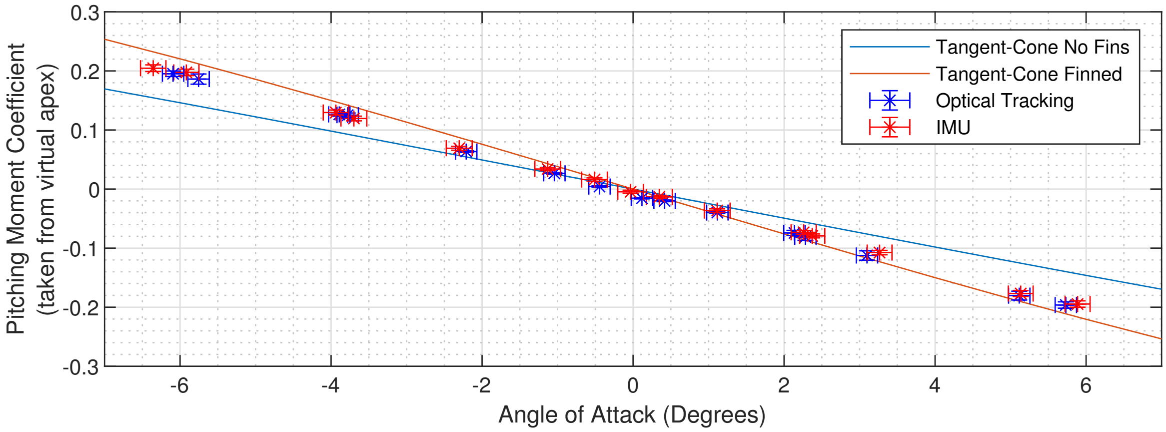

Fig. 13 Pitching moment coefficient at Mach 7 condition. Individual tests plotted against tangent-cone numerical prediction

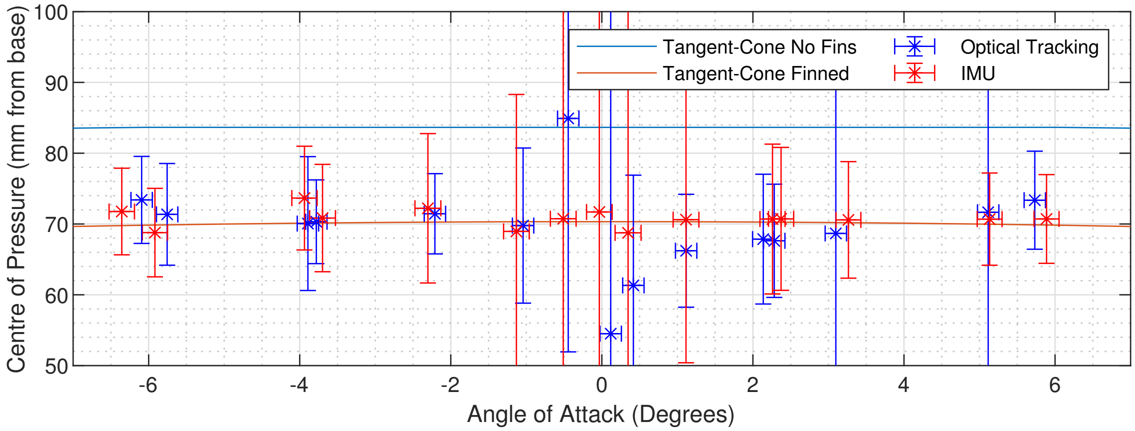

Fig. 14 Centre of Pressure Location (from cone base) at Mach 7 condition. Individual tests plotted against tangent-cone numerical prediction

B. Roll Moment Coefficient

A final set of experiments were conducted to examine the rolling moment coefficient of the model. The free-flight model was designed to allow for fins that had deflections of up to 3 °. Angling the fins in the same direction will produce a rolling moment upon flow initiation, causing the cone to spin. The equation of for roll moment coefficient is:

$$C_l = \frac{I_{xx}\ddot{\phi}}{\overline{q}Sc} \tag{7}$$

Figure 15 shows an example roll test where all the fins were angled at 3 °. Image tracking is not used for these tests as the model did not feature appropriate markings required to track roll. It can be seen that for the first two cone frames on the composite image that the tunnel is yet to have fired so the cone remains at 0 ° roll. After reaching the centreline of the core flow, the facility has fired and the cone begins to roll. By the end of the test time, the angular velocity has reached 2000 °/s, saturating the gyroscopes of the IMU.

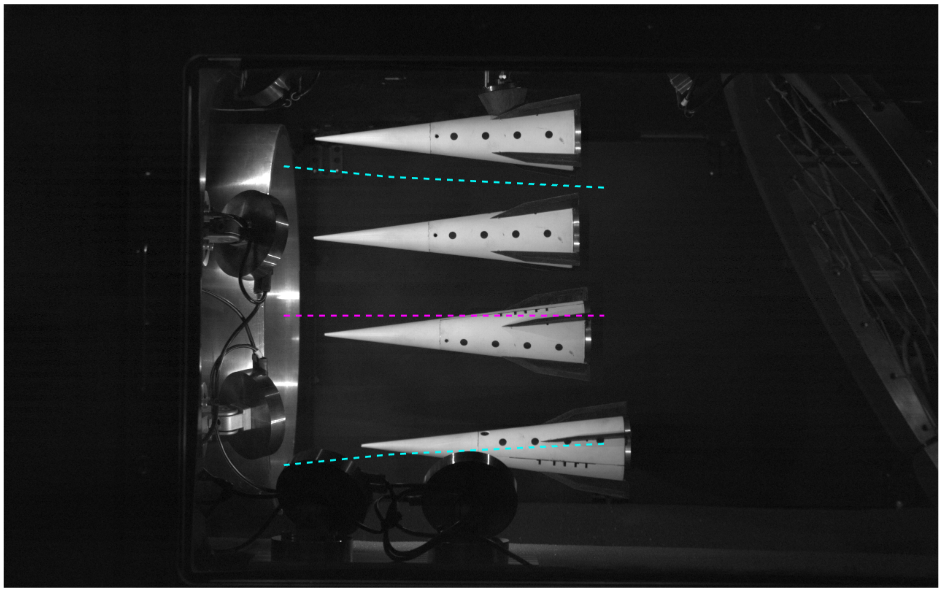

Fig. 15 Composite image of rolling finned cone (cyan - core flow location as acquired by a pitot survey, pink - nozzle centreline).

In total, 5 spin test were conducted in free-flight at zero degrees angle of attack. One with no fin deflections, 2 fins at ± 3 ° and 4 fins at ± 3 °. Figure 16 shows the measured transient roll coefficient for all 5 experiments with the test time overlaid. The signals contain some noise as the roll angular velocity is differentiated to obtain the acceleration to calculate the roll coefficient. For the cases where four fins are deflected, the gyroscope saturates just after the end of the test time as seen in the figure. The results show good symmetry between the cases where the roll direction is opposite and in each test steady state is achieved within the available test flow duration. The maximum uncertainty was calculated to be ± 0.0452 using error propagation. As a percentage, this is a larger uncertainty than the force coefficients due to the requirement of differentiating the angular velocity measured by the IMU. These results show that it is possible to reliably measure roll coefficient in free-flight.

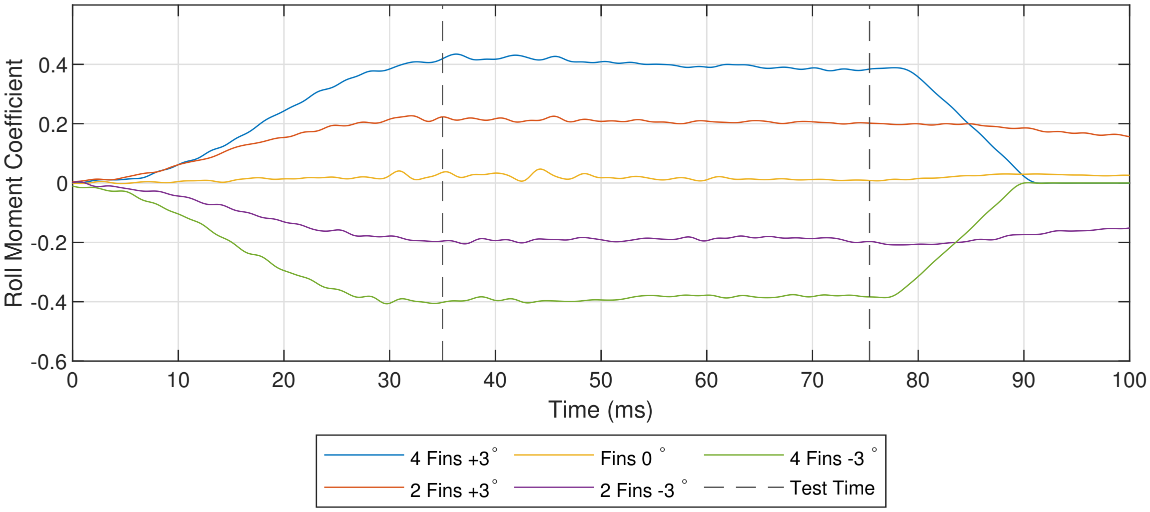

Fig. 16 Roll Coefficient at Mach 7 condition for various fin deflections

VI. Conclusions

The static longitudinal and roll aerodynamic coefficients for a finned cone have been measured using the free-flight technique in the University of Oxford HDT. The finned cone adds the complexity of a varying centre of pressure position with angle of attack making it more challenging to achieve the quasi-static free-flight condition as the centre of gravity needs to be adjusted when a new angle of attack is tested. Nevertheless, high quality aerodynamic data were obtained Lift and drag coefficient exhibited the expected shapes with respect to angle of attack and agree well with the numerical predictions. However, care must be taken with image tracking if there is slight roll in an experiment, particularly for drag coefficient. Furthermore, the two independent methods of measuring accelerations, image tracking and an on-board IMU, show very good agreement in the experimental data, adding redundancy to the overall free-flight methodology. It has also been shown for the first time that the free-flight technique can be used to obtain high quality roll moment coefficient data. Overall, the static free-flight technique has been validated for a complex body with non-constant centre of pressure with angle of attack which gives a high degree of confidence for obtaining static aerodynamic coefficients for any hypersonic vehicle geometry.

VII. Acknowledgments

This research was funded and supported by DSTL. The authors would like to thank Trevor Birch (DSTL) for his technical support of the research. The authors would like to acknowledge the exhaustive work of Tristan Crumpton for operating the HDT during testing. We would also like to thank Prof. Andrew Neely and Mr Liam McQuellin from UNSW Canberra for supplying the free-flight DAQs.

References

[1] Wuilbercq, R., Pescetelli, F., Minisci, E., and Brown, R. E., "Influence of Boundary Layer Transition on the Trajectory Optimisation of a Reusable Launch Vehicle," *19th AIAA International Space Planes and Hypersonic Systems and Technologies Conference*, 2014, p. 2362. https://doi.org/https://doi.org/10.2514/6.2014-2362.

[2] Stetson, K. F., "Hypersonic boundary-layer transition," *Advances in Hypersonics*, 1992, pp. 324–417.

[3] Juhany, K. A., and Darji, A., "Force Measurement in a Ludwieg Tube Tunnel," *Journal of Spacecraft and Rockets*, Vol. 44, No. 1, 2007, pp. 88–93. https://doi.org/10.2514/1.21014.

[4] Sanderson, S. R., and Simmons, J. M., "Drag balance for hypervelocity impulse facilities," *AIAA journal*, Vol. 29, No. 12, 1991, pp. 2185–2191.

[5] Mee, D. J., Daniel, W. J. T., and Simmons, J. M., "Three-component force balance for flows of millisecond duration," *AIAA journal*, Vol. 34, No. 3, 1996, pp. 590–595.

[6] Doherty, L. J., Smart, M. K., and Mee, D., "Measurement of three-components of force on an airframe integrated scramjet at Mach 10," *20th AIAA International Space Planes and Hypersonic Systems and Technologies Conference*, 2015, p. 3523.

[7] Pick, G. S., "Sting Effects in Hypersonic Base Pressure Measurements," Tech. rep., TR AL-85, Dec. 1971, Naval Ship Research and Development Center , Bethesda, Md., 1971.

[8] Bernstein, L., and Pankhurst, R. C., "Force measurements in short-duration hypersonic facilities," Tech. rep., 1975.

[9] Dayman Jr, B., "Free-flight testing in high-speed wind tunnels," Tech. rep., 1966.

[10] Leiser, D., Löhle, S., Zander, F., Buttsworth, D. R., Choudhury, R., and Fasoulas, S., "Analysis of Reentry and Break-Up Forces from Impulse Facility Experiments and Numerical Rebuilding," *Journal of Spacecraft and Rockets*, 2022, pp. 1–13.

[11] Grossir, G., Puorto, D., Ilich, Z., Paris, S., Chazot, O., Rumeau, S., Spel, M., and Annaloro, J., "Aerodynamic characterization of space debris in the VKI Longshot hypersonic tunnel using a free-flight measurement technique," *Experiments in Fluids*, Vol. 61, No. 7, 2020. https://doi.org/10.1007/s00348-020-02995-7.

[12] Park, S. H., and Park, G., "Separation process of multi-spheres in hypersonic flow," *Advances in Space Research*, Vol. 65, No. 1, 2020, pp. 392–406. https://doi.org/10.1016/j.asr.2019.10.009, URL https://doi.org/10.1016/j.asr.2019.10.009.

[13] Seltner, P. M., Willems, S., and Gülhan, A., "Aerodynamic coefficients of free-flying cubes in hypersonic flowfield," *Journal of Spacecraft and Rockets*, Vol. 56, No. 6, 2019, pp. 1725–1734.

[14] Seltner, P. M., Willems, S., Gülhan, A., Stern, E. C., Brock, J. M., and Aftosmis, M. J., "Aerodynamics of inclined cylindrical bodies free-flying in a hypersonic flowfield," *Experiments in Fluids*, Vol. 62, No. 9, 2021, p. 182.

[15] Kovács, D. G., Grossir, G., Dimitriadis, G., and Chazot, O., "Space debris interaction across a two-dimensional oblique shock wave," *Experiments in Fluids*, Vol. 64, No. 8, 2023, p. 146.

[16] Tanno, M., and Tanno, H., "Aerodynamic characteristics of a free-flight scramjet vehicle in shock tunnel," *Experiments in Fluids*, Vol. 62, No. 7, 2021, pp. 1–12.

[17] Tanno, H., Komuro, T., Sato, K., Fujita, K., and Laurence, S. J., "Free-flight measurement technique in the free-piston high-enthalpy shock tunnel," *Review of scientific instruments*, Vol. 85, No. 4, 2014, p. 45112.

[18] Laurence, S. J., Butler, C. S., Martinez Schramm, J., and Hannemann, K., "Force and moment measurements on a free-flying capsule in a shock tunnel," *Journal of Spacecraft and Rockets*, Vol. 55, No. 2, 2018, pp. 403–414.

[19] Mudford, N. R., O'Byrne, S., Neely, A., Buttsworth, D., and Balage, S., "Hypersonic Wind-Tunnel Free-Flying Experiments with Onboard Instrumentation," *Journal of Spacecraft and Rockets*, 2015. https://doi.org/10.2514/1.A32887.

[20] Kennell, C., Neely, A. J., Buttsworth, D. R., Choudhury, R., and Tahtali, M., "Free Flight Testing in Hypersonic Flows: HEXAFLY-INT EFTV," *54th AIAA Aerospace Sciences Meeting*, 2016, p. 1152. https://doi.org/https://doi.org/10.2514/6.2016-1152.

[21] Kennell, C., Reimann, B., Choudhury, R., Buttsworth, D., and Neely, A., "Subscale hypersonic free flight dynamics of HEXAFLY-INT EFTV+ ESM (multibody separation)," *7th European Conference for Aeronautics and Space Science*, 2017.

[22] McQuellin, L. P., Kennell, C. M., Neely, A. J., Sytsma, M. J., Silvester, T., Choudhury, R., and Buttsworth, D. R., "Investigating endo-atmospheric separation of a hypersonic flyer-sustainer using wind tunnel based free-flight," *23rd AIAA International Space Planes and Hypersonic Systems and Technologies Conference, 2020*, 2020, pp. 1–24. https://doi.org/10.2514/6.2020-2451.

[23] Hyslop, A., Doherty, L. J., McGilvray, M., Neely, A., McQuellin, L. P., Barth, J., and Mullen, G., "Free-Flight Aerodynamic Testing of the Skylon Space Plane," *Journal of Spacecraft and Rockets*, 2021, pp. 1–11.

[24] Hyslop, A. M., McGilvray, M., and Doherty, L. J., "Free-Flight Aerodynamic Testing of a 7 Degree Half-Angle Cone," *AIAA SCITECH 2022 Forum*, 2022, p. 1324.

[25] Hyslop, A. M., "Force measurement techniques in short duration hypersonic facilities," , 2023.

[26] McGilvray, M., Doherty, L. J., Neely, A. J., Pearce, R., and Ireland, P., "The Oxford High Density Tunnel," *20th AIAA International Space Planes and Hypersonic Systems and Technologies Conference*, 2015, p. 3548. https://doi.org/https://doi.org/10.2514/6.2015-3548.

[27] Wylie, S., Doherty, L., and McGilvray, M., "Commissioning of the Oxford High Density Tunnel (HDT) for Boundary Layer Instability Measurements at Mach 7," *2018 Fluid Dynamics Conference*, 2018, p. 3074. https://doi.org/https://doi.org/10.2514/6.2018-3074.

[28] Hunter, D., "UK Hypersonic Glide Vehicle Concept and Performance Assessment," *RAeS Weapon Systems and Technology*, 2019.

[29] Keyes, F. G., "A Summary of Viscosity and Heat-Conduction Data for He, A, H2, O2, CO, CO2, H2O, and air," *Transactions of the ASME*, Vol. 73, 1951, pp. 589–596.

[30] Oceanic, U. S. N., Administration, A., and Force, U. S. A., *US standard atmosphere, 1976*, Vol. 76, National Oceanic and Atmospheric Administration, 1976.

[31] Wheeler, C., Hyslop, A., Vieira, J., Page, L. L., Quinn, M. K., and Nafiz, H. K., "HiSST : 2nd International Conference on High-Speed Vehicle Science Technology Surface Pressure Measurements on a Free-Flying Cone at Mach 7 using Pressure Sensitive Paint," , No. September, 2022, pp. 1–19.

[32] Kennell C, "Study of Hypersonic Aerodynamics Using Free Flight Experiments," Tech. rep., 2018.

[33] Canny, J., "A Computational Approach to Edge Detection," *IEEE Transactions on Pattern Analysis and machine Intelligence*, Vol. PAMI-8, No. 6, 1986, pp. 679–698.

[34] Hough, P. V. C., "Method and Means for Recognizing Complex Patterns," , dec 1962.

[35] von Gioi, R. G., and Randall, G., "A Sub-Pixel Edge Detector: an Implementation of the Canny/Devernay Algorithm." *IPOL Journal*, Vol. 7, 2017, pp. 347–372.

[36] Laurence, S. J., and Hornung, H. G., "Image-Based Force and Moment Measurement in Hypersonic Facilities," *Experiments in Fluids*, Vol. 46, No. 2, 2009, pp. 343–353.

[37] Moffat, R. J., "Describing the uncertainties in experimental results," *Experimental thermal and fluid science*, Vol. 1, No. 1, 1988, pp. 3–17.